*Burns & Trauma*, 2024, 12, tkae045
https://doi.org/10.1093/burnst/tkae045
Research Article

OXFORD

Research Article

# Glutamine promotes the proliferation of intestinal stem cells via inhibition of TP53-induced glycolysis and apoptosis regulator promoter methylation in burned mice

**Panyang Zhang[1], Dan Wu[1], Xule Zha[1], Sen Su[1], Yajuan Zhang[1], Yan Wei[1], Lin Xia[1] and Shijun Fan[1], and Xi Peng[1,2,*]**

[1]Clinical Medical Research Center, Southwest Hospital, Third Military Medical University (Army Medical University), Gaotanyan Street, Shapingba District, Chongqing, 400038, China and [2]State Key Laboratory of Trauma and Chemical Poisoning, Southwest Hospital, Third Military Medical University (Army Medical University), Gaotanyan Street, Shapingba District, Chongqing, 400038, China

*Corresponding author. E-mail: pxlrmm@tmmu.edu.cn

Received 1 January 2024; Revised 8 April 2024; Editorial decision 8 July 2024

## Abstract

**Background:** Intestinal stem cells (ISCs) play a pivotal role in maintaining intestinal homeostasis and facilitating the restoration of intestinal mucosal barrier integrity. Glutamine (Gln) is a crucial energy substrate in the intestine, promoting the proliferation of ISCs and mitigating damage to the intestinal mucosal barrier after burn injury. However, the underlying mechanism has not yet been fully elucidated. The objective of this study was to explore the mechanism by which Gln facilitates the proliferation of ISCs.

**Methods:** A mouse burn model was established to investigate the impact of Gln on intestinal function. Subsequently, crypts were isolated, and changes in TP53-induced glycolysis and apoptosis regulator (TIGAR) expression were assessed using real-time quantitative polymerase chain reaction (RT-qPCR), western blotting, immunohistochemistry, and immunofluorescence. The effects of TIGAR on cell proliferation were validated through CCK-8, EdU, and clonogenicity assays. Furthermore, the effect of TIGAR on Yes-associated protein (YAP) nuclear translocation and ferroptosis was examined by western blotting and immunofluorescence staining. Finally, dot blot analysis and methylation-specific PCR were performed to evaluate the effect of Gln on TIGAR promoter methylation.

**Results:** The mRNA and protein levels of TIGAR decreased after burn injury, and supplementation with Gln increased the expression of TIGAR. TIGAR accelerates the nuclear translocation of YAP, thereby increasing the proliferation of ISCs. Concurrently, TIGAR promotes the synthesis of nicotinamide adenine dinucleotide phosphate (NADPH) and glutathione to suppress ferroptosis in ISCs. Subsequent investigations demonstrated that Gln inhibits TIGAR promoter methylation by increasing the expression of the demethylase ten-eleven translocation. This change increased TIGAR transcription, increased NADPH synthesis, and reduced oxidative stress, thereby facilitating the restoration of intestinal mucosal barrier integrity post-burn injury.

**Conclusions:** Our data confirmed the inhibitory effect of Gln on TIGAR promoter methylation, which facilitates YAP translocation into the nucleus and suppresses ferroptosis, ultimately promoting the proliferation of ISCs.

## Graphical Abstract

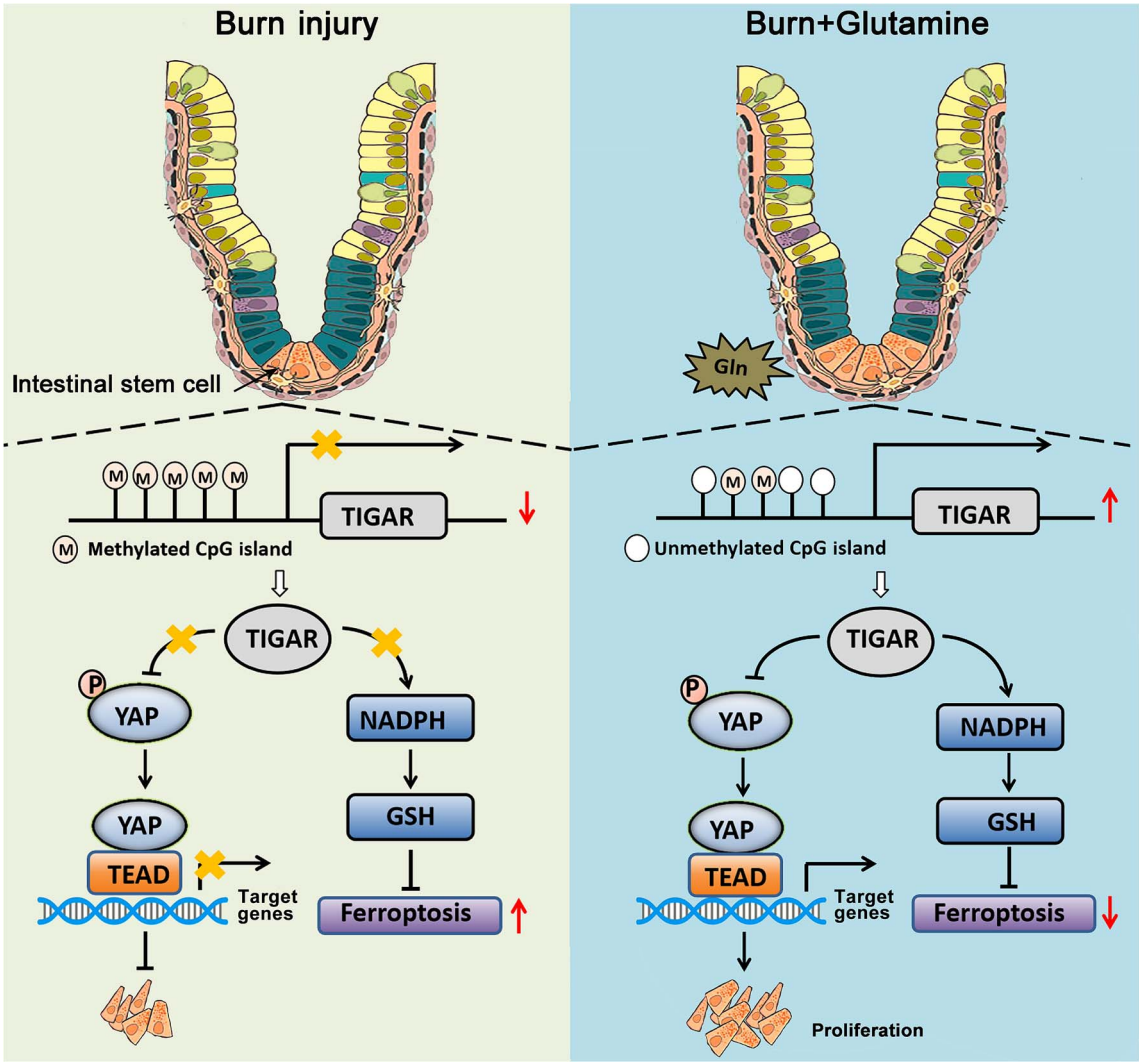


**Key words:** Burn injury, Intestinal stem cells, Glutamine, TP53-induced glycolysis and apoptosis regulator, Methylation, Proliferation, Ferroptosis

## Highlights

- Glutamine facilitates intestinal stem cell proliferation by promoting TIGAR expression through inhibition of the methylation of its promoter.
- TIGAR facilitates the proliferation of intestinal stem cells by promoting the translocation of Yes-associated protein into the nucleus and suppressing ferroptosis by increasing the synthesis of nicotinamide adenine dinucleotide phosphate and glutathione.

## Background

Extensive burn injury is a highly critical form of trauma that poses a major threat to human health [1]. Burn stress, tissue ischemia and hypoxia-induced damage, as well as an exaggerated inflammatory response, can contribute to the development of multiple organ dysfunction syndrome [2,3]. The intestinal tract is particularly susceptible to damage after burn injury due to the unique distribution of its villous vessels [4,5]. Impairment of the intestinal mucosal barrier serves as the pathophysiological basis for enterogenic infection and enterogenous hypermetabolism [6,7]. Strategies to effectively mitigate intestinal mucosal injury and promote repair are important clinical concerns in burn care. The intestine has developed a highly efficient self-repair mechanism throughout the course of evolution to effectively counteract various types of pathological damage. The renewal of intestinal epithelial cells relies on intestinal stem cells (ISCs) located at the base of the crypts [8]. Following injury-induced stimulation of the intestine, ISCs strongly proliferate to ensure a consistent population of intestinal epithelial cells, maintaining a balance between regeneration and apoptosis [9]. The metabolism of ISCs is vigorous and relies on an adequate nutrient supply and the maintenance of redox homeostasis in the microenvironment [10,11].

Severe burns can induce metabolic disorders and oxidative stress, which may impede the proliferation of ISCs, leading to delayed repair of damaged intestinal mucosa [12]. The essential role of glutamine (Gln) and glucose as the primary energy substrates for ISCs has been established, and these molecules are indispensable for maintaining the physiological function of these cells [13,14]. Furthermore, Gln plays a pivotal role in maintaining the cellular redox balance, which has attracted increasing attention for its impact on stem-cell functionality [15]. A reduction in the plasma Gln concentration post-burn injury is a crucial factor that leads to the delayed restoration of injured intestinal mucosa [16]. Gln serves not only as an energy source for intestinal epithelial cells but also as a nitrogen provider for protein and nucleic acid synthesis; thus, Gln is a special nutrient necessary for the proliferation of vigorous cells [17,18]. Recent studies have revealed that Gln increases the activity of glucose-6-phosphate dehydrogenase (G6PD), which is the rate-limiting enzyme in the glucose pentose phosphate pathway (PPP), thereby facilitating the synthesis of nicotinamide adenine dinucleotide phosphate (NADPH), a pivotal reducing agent crucial for maintaining cellular redox balance and accelerating the repair of damaged mucosa [19]. However, it is currently unclear whether Gln can promote the entry of glucose into the PPP.

In recent years, TP53-induced glycolysis and apoptosis regulator (TIGAR) has attracted increasing attention as a metabolic regulatory enzyme that promotes glucose entry into the PPP. TIGAR inhibits glycolysis by facilitating the reverse conversion of fructose 1–6 diphosphate into fructose 6-phosphate, thereby diverting glucose from the glycolytic pathway toward the PPP [20]. Consequently, TIGAR is a pivotal regulator controlling glucose metabolism and flux. Whether the effect of Gln on glucose metabolism is related to TIGAR has not been reported. Evidence has shown that Gln promotes PPP metabolism by activating G6PD and increases glucose flux toward the hexosamine biosynthesis pathway [19,21]. Thus, Gln may regulate TIGAR, thereby affecting glucose metabolism. To date, information on the regulation of TIGAR post-burn injury and the regulatory effects of Gln is lacking. This study aimed to identify TIGAR as a novel target for the regulation of glucose metabolism by Gln, thereby increasing our understanding of how Gln maintains intestinal mucosal barrier function.

## Methods

### Animals

Five-week-old male BALB/c mice, which were utilized for the establishment of experimental animal models, were procured from the Laboratory Animal Center of the Third Military Medical University and housed in specific pathogen-free-grade animal facilities of the Clinical Medical Research Center, Southwest Hospital of Third Military Medical University. The mice were acclimated to the environment for 1 week prior to burn-model construction. All animal experiments were conducted in strict accordance with the national and Third Military Medical University guidelines for the use of experimental animals and were approved by the Medical Ethics Committee of the Third Military Medical University.

### Murine model of burn injury

We constructed a burn mouse model as described in a previous study [22]. Briefly, mice with similar weights were anesthetized with ketamine (80 mg/kg) and xylazine (10 mg/kg) and divided into three groups: the sham group, burn group and burn+Gln group. The hair on the back was shaved with a razor, and the excess hair was wiped off after the depilatory paste was applied to fully expose the backs of the mice. The mice were positioned in a specialized concave mold with their dorsal side facing downward, ensuring that the back region, which constituted ~30% of the mouse total body surface area (TBSA), extended beyond the bottom surface of the mold. The water-bath interface was adjusted to align precisely with the bottom of the mold, and the water temperature was elevated to 95°C. Subsequently, the mice were immobilized within the mold and immersed in a water bath for 10 s; the mice that were immersed in a 37°C water bath for 10 s were defined as the sham group. Next, the dorsal region of each mouse was delicately dried via gentle wiping and injected with 1.5 ml * kg * %TBSA lactated Ringer's solution for fluid resuscitation and 100 $\mu$l of buprenorphine (0.3 mg/ml) for analgesia. The mice were maintained at 37°C for 48 h. Then, the mice were intraperitoneally injected twice daily for 7 days with 0.3 ml of saline (sham and burn groups) or 1 g/kg body weight of Gln in 0.3 ml of saline (burn + Gln group). After injection for 1, 3, 5 or 7 days, the mice were euthanized by cervical dislocation. Then, the abdomen was opened aseptically through a midline laparotomy and the distal colon was aseptically harvested.

The experimental design is shown in Figure S1, see online supplementary material.

### Cell lines and culture

The rat small intestinal epithelial cell line IEC-6 was obtained from American Type Culture Collection (ATCC), while 293 T cells were maintained in our laboratory. Both cell lines were cultured in Dulbecco's modified Eagle's medium (DMEM; Gibco, USA) supplemented with 10% fetal bovine serum (Gibco, USA) at 37°C and 5% $CO_2$ in an incubator. For simulation of the inflammatory state after burn injury, the cells were treated with lipopolysaccharide (LPS) (10 $\mu$g/ml, Sigma, USA) for 24 h, and the concentration of added Gln (Sigma, USA) was 2 mM; the cells not treated with LPS and Gln were defined as the control group.

### Hematoxylin and eosin staining and histological scoring

The small intestinal tissues of the mice were collected at various time points and fixed with 4% paraformaldehyde. Subsequently, the small intestinal samples were embedded in paraffin and sectioned into 5 $\mu$m slices. Following dewaxing, the paraffin sections were stained with hematoxylin and eosin. Microscopic examination was performed to evaluate the staining effect, allowing observation of morphological changes in intestinal villi and crypts within each experimental group.

The histological examination was performed using a previously validated and described scoring system [19] as follows: tissue damage, 0 (none) to 3 (extensive mucosal damage); crypt length, 0 (normal) to 4 (significantly shortened); and villus damage, 0 (none) to 4 (extensive swelling collapse). The lengths of the crypts and villi were measured using Cell-Sens software (Olympus).

### *In vivo* intestinal permeability assay

We tested intestinal permeability using a 4-kDa fluorescein isothiocyanate-dextran (FITC-dextran) assay as previously described [23]. Briefly, 4 h prior to euthanasia, mice were given an oral gavage of 600 mg/kg body weight 4-kDa FITC-dextran (Sigma, USA) in sterile phosphate-buffered saline (PBS) solution. At the time of euthanasia, blood was extracted by cardiac puncture. FITC-dextran levels in serum were measured in technical duplicates using a fluorescence spectrophotometer (Varioskan Flash, Thermo Fisher, USA) (excitation, 490 nm; emission, 520 nm) and quantified based on a standard curve. Standard curves for calculating the FITC-dextran concentration were obtained by diluting FITC-dextran in PBS.

### Crypt isolation and culture

Fresh small-intestinal tissue was collected from the mice and subsequently rinsed with normal saline to eliminate contaminants. The small intestine was then longitudinally incised using sterile scissors, followed by gentle irrigation of the inner wall of the small intestine with saline 7–8 times until all discernable contents were thoroughly eliminated. The small intestine was sectioned into 0.5 cm segments and placed in a centrifuge tube containing 40 ml of sterile chelating agent containing 10 mM Ethylene Diamine Tetraacetic Acid (EDTA) and Ethylene Glycol Tetraacetic Acid (EGTA) (Solarbio, China), 2% sorbitol (Solarbio, China), 1% sucrose (Solarbio, China) or 100 U/ml Pen/Strep (Beyotime, China) on a shaking table at 4°C for 30 min. The centrifugal tube was vertically oscillated by the arm to facilitate separation of the crypt, and subsequently, the recess suspension was filtered through a 70 $\mu$m filter for impurity removal. Then, the filtrate was centrifuged at 700 rpm and maintained at 4°C for 10 min. The supernatant was discarded, and the precipitate were crypts.

The obtained crypts were resuspended in 40 ml of sterile PBS containing BSA and then centrifuged at 700 rpm at 4°C for 5 min. The supernatant was subsequently discarded. Then, these crypts were resuspended in 0.5 ml of washing medium containing DMEM/F12 medium supplemented with 1% Pen/Strep, 1× GlutaMAX (Thermo, USA) and 1 mM *N*-acetyl-L-cysteine (Sigma, USA). The total number of crypts required was calculated based on the desired number of crypts per well [10–30/10 $\mu$l of Matrigel (Invitrogen, USA)/96 wells]. Subsequently, the corresponding volume of the crypt suspension was collected and centrifuged at 700 rpm for 5 min at 4°C. After the supernatant was discarded, an equivalent volume of Matrigel was added to reintroduce the crypt. The Matrigel was carefully dispensed into the center of each well in a 96-well plate at a volume of 10 $\mu$l per well and then immediately placed in a 37°C incubator for 15 min. Subsequently, the culture plate was retrieved and supplemented with 200 $\mu$l of DMEM/F12 with 1× B27 supplement (Gibco, USA), 1× N2 supplement (Gibco, USA), 1× GlutaMAX, and 1% Pen/Strep and 10 $\mu$M Y27632 (Selleck, USA); the medium was refreshed every 2 days. The organoids were treated with LPS (10 $\mu$g/ml, Sigma, USA) for 48 h and the concentration of the supplemented Gln (Sigma, USA) was 2 mM.

### Plasmid construction, lentivirus packaging and infection

The TIGAR coding sequence (CDS) region sequence was retrieved from the Ensembl database and primers were designed for its amplification. The primers were subsequently ligated to the lentiviral vector plasmid pCDH-EF1-MCS-T2A-Puro (Tsingke, China) following enzymatic digestion. Mock plasmids lacking TIGAR CDSs were used as negative controls. For knockdown of TIGAR, four short hairpin RNAs (shRNAs) and one shNC control plasmid were procured from Tsingke Biotech. For establishment of stable cell lines with TIGAR overexpression or knockdown, 293 T cells were transfected with plasmids for overexpression or knockdown along with two helper plasmids. The resulting viral supernatant was collected after 48 h and subsequently used to infect IEC-6 cells. Finally, the infected cells were selected using puromycin.

### RNA isolation and real-time quantitative polymerase chain reaction

Total RNA from crypts or IEC-6 cells was extracted using TRIzol (TaKaRa, Japan), and its purity and concentration were assessed using a Nanodrop2000 system. Subsequently, reverse transcription of total RNA into cDNA was performed utilizing a reverse transcription kit (TaKaRa, Japan). Finally, real-time quantitative polymerase chain reaction (RT-qPCR) analysis was conducted with TB Green (TaKaRa, Japan), and the relative gene expression was calculated using the $2^{-\Delta\Delta CT}$ method. The sequences of the primers used in this study are shown in Table S1, see online supplementary material.

### DNA isolation and methylation-specific PCR

Genomic DNA was extracted from crypts and cells using a TIANamp Genomic DNA Kit (Tiangen, China) according to the manufacturer's protocols. The concentration and purity of the DNA were determined using a Nanodrop2000 system, while TIGAR promoter methylation was assessed using a DNA methylation kit (Beyotime, China). In brief, TIGAR promoter cytosine-phosphate-guanine islands were identified using the MethPrimer database (http://www.urogene.org/methprimer/), and corresponding methylation PCR primers were synthesized; these sequences are shown in Table S1. DNA modification was carried out using sodium bisulfite, after which the modified DNA was purified, and subsequent methylation-specific PCR was performed using specific primers and EpiTaq™ HS (TaKaRa, Japan). Finally, the amplification products were analyzed via agarose-gel electrophoresis.

### Dot blot

Genomic DNA was extracted using Tris-EDTA (TE) buffer and diluted to a concentration of 50–200 ng/$\mu$l. The diluted DNA was denatured at 95°C for 10 min, followed by cooling on ice for 5 min. Subsequently, a nitrocellulose membrane was cut to the desired size, and 1–2 $\mu$l of the sample was spotted onto it. After air-drying, the membrane was incubated at 60°C for 1–2 h. Next, the membrane was blocked with a solution containing 5% BSA for 1 h before being incubated overnight at 4°C with a primary antibody against 5-methylcytosine (5mC; 1 : 1000, Active Motif, USA) or 5-hydroxymethylcytosine (5hmC; 1 : 5000, Active Motif, USA). After being washed with TBST, the membrane was incubated with a secondary antibody at room temperature for 1 h and then exposed to enhanced chemiluminescence reagent.

### Western blot

Protein extraction reagent (Thermo Fisher Scientific, USA) supplemented with 1× protease and phosphatase inhibitors was used for the isolation of total protein from tissues and cells, and the protein concentration was then determined using the BCA method (Beyotime, China). Subsequently, protein loading buffer was added and the samples were subjected to heating at 100°C for 5 min. The protein was subsequently transferred to a PVDF membrane (Millipore, USA) following SDS-PAGE and then incubated at room temperature for 2 h in 5% skim milk or BSA (for phosphorylated protein). Subsequently, the membrane was incubated overnight at 4°C with diluted primary antibodies against TIGAR (1 : 2000, Santa Cruz, USA), Yes-associated protein (YAP; 1 : 3000, Proteintech, China), phosphorylated YAP (p-YAP; 1:3000, Abcam, UK), glutathione peroxidase 4 (GPX4; 1:5000, Abcam, UK), leucine-rich repeat-containing G protein-coupled receptor 5 (Lgr5; 1:1000, Beyotime, China), proliferating cell nuclear antigen (PCNA; 1:3000, Proteintech, China) and GAPDH (1:5000, Proteintech, China). The membrane was washed three times with TBST for 10 min each time and then incubated with an HRP-conjugated secondary antibody (1 : 5000, Cell Signaling, USA) at room temperature for 2 h. Finally, enhanced chemiluminescence luminescent solution (Solarbio, China) was used for signal development.

### Immunofluorescence

The cells were inoculated into 24-well plates with coverslips and treated with LPS or Gln for 24 h. Subsequently, the cells were washed with PBS, fixed with 4% paraformaldehyde for 15 min and then washed three times with PBS. Permeabilization was achieved by incubating the cells at room temperature for 15 min in a solution of 0.5% Triton X-100 prepared in 1× PBS. Following this step, the slides were treated with 5% BSA and sealed at room temperature for 1 h. Next, diluted primary antibodies against TIGAR (1 : 100, Santa Cruz, USA), Lgr5 (1 : 100, Beyotime, China) and Ki67 (1:100, Thermo Fisher Scientific, USA) were added to the slides, which were then placed in a humidified chamber overnight at 4°C. After PBS washes, the cells were incubated with a fluorescent secondary antibody in a humidified chamber at 37°C for 1 h in the absence of light. Subsequently, DAPI was added and the cells were incubated for 5 min in the dark. Finally, the slides were sealed using an antifluorescent quenching agent-containing sealing solution and the resulting images were visualized using a confocal microscope.

### Immunohistochemical staining

The paraffin sections were dewaxed using xylene and gradient alcohol, followed by sodium citrate treatment for antigen retrieval. Subsequently, the tissues were permeabilized with PBS containing 0.5% Triton X-100 at room temperature and blocked with 0.5% BSA for 1 h. Next, the primary antibody against TIGAR (1 : 100, Santa Cruz, USA) working solution was added and incubated overnight at 4°C, followed by incubation with a fluorescent secondary antibody at room temperature for 1 h. DAPI working solution was then applied before the sections were sealed with an antifluorescence quenching solution. Finally, confocal imaging was performed.

### Cytoplasmic and nuclear fractionation

Cytoplasmic and nuclear fractionation was performed using the PARIS™ kit (Thermo Fisher Scientific, USA). Briefly, the

cells were gently scraped off using a cell scraper, washed with PBS and placed on ice. Next, 200 $\mu$l of cell fractionation buffer was added for every 20 $\mu$l of cell precipitation, and the cells were gently resuspended by vortexing or pipetting and incubated on ice for 5 min. Then, the samples were centrifuged for 5 min at 4°C and 500 × g. The supernatant contained cytoplasmic protein and the pellet was the nuclear fraction. Next, a volume of cell disruption buffer equal to the volume of cell fractionation buffer was added to the nuclear fraction, which was vortexed or pipetted vigorously to lyse the nuclei. Then, the samples were centrifuged for 5 min at 4°C and 500 × g, the supernatant contained the nuclear protein, and subsequently, the cytoplasmic and nuclear proteins were subjected to western blot analysis.

### NADPH/NADP$^+$ and glutathione/oxidized glutathione ratio assays

The NADPH/NADP$^+$ ratios in intestinal crypts and cultured cells were determined with a commercial kit (Beyotime, China). In brief, 200 $\mu$l of NADPH/NADP$^+$ extraction buffer was added to a 6-well plate to facilitate cellular lysis. After centrifugation at 12 000 × g and 4°C for 5 min, the supernatant was collected for analysis. Then, a standard curve was generated according to the instructions. $NADP_{total}$ was determined first, and then, the concentration of NADPH in the sample was determined after the sample was incubated in a water bath at 60°C for 30 min to decompose NADP$^+$. The NADPH/NADP$^+$ ratio was calculated according to the following formula: NADPH/NADP$^+$ = ($NADP_{total}$ − NADP$^+$)/NADP$^+$. The glutathione/oxidized glutathione (GSH/GSSG) ratio in intestinal crypts and cultured cells was determined by a commercial kit (Beyotime, China) according to the manufacturer's instructions. The concentrations of GSH and GSSG were calculated using a standard curve.

### Iron assay

The iron levels in IEC-6 cells and crypts were determined using a Cell Ferrous Iron Colorimetric Assay Kit (Elabscience, China) according to the manufacturer's instructions. In brief, the cells were quickly homogenized with iron assay buffer, lysed on ice for 10 min and centrifuged for another 10 min at 15 000 × g, after which the supernatant was collected for the next step. Then, 80 $\mu$l of various concentrations of standard products and test samples was added to the wells of the enzyme-labeled plate, followed by the addition of 80 $\mu$l of iron-determination buffer. The contents were thoroughly mixed and incubated at 37°C for 10 min. The optical density (OD) of each well was measured at 593 nm. The concentration of iron was calculated using the standard curve and is expressed as nmol of $Fe^{2+}$ per $10^6$ cells or $\mu$mol of $Fe^{2+}$ per kg wet weight.

### Quantification of reactive oxygen species

For analysis of reactive oxygen species (ROS), IEC-6 cells were incubated with 10 $\mu$M H2DCFDA (MCE, USA) at 37°C for 30 min. Subsequently, the cells were washed with PBS three times, digested with pancreatic enzymes and then resuspended in complete medium for analysis by flow cytometry.

### Statistical analysis

Statistical analyses were performed with SPSS 19.0 (IBM, SPSS, Chicago, IL, USA) and GraphPad Prism 5.0. The Shapiro–Wilk normality test was performed to determine the data distribution. Normally distributed data are reported as the mean ± standard deviation and non-normally distributed data are reported as the median with interquartile range. Student's t test was used for differences between two groups. One-way analysis of variance (ANOVA) with Bonferroni correction and the Kruskal–Wallis test (non-normal distribution or unequal variance) were performed for comparisons between multiple groups. $P$ values $< 0.05$ were considered to indicate statistical significance. For all the statistical analyses, $^*p < 0.05$, $^{**}p < 0.01$ and $^{***}p < 0.001$.

## Results

### Supplementation with Gln mitigated burn-induced intestinal injury in mice

The impact of Gln on the restoration of the intestinal mucosal barrier was investigated in a murine burn-injury model. Compared with the sham group, the burn group exhibited significant hemorrhage on the mucosal surface of the small intestine. Notably, these alterations were effectively ameliorated upon Gln supplementation (Figure 1a). In addition, intestinal permeability was found to be increased following burn injury, whereas Gln supplementation resulted in a reduction in intestinal permeability (Figure S2, see online supplementary material). Subsequent hematoxylin and eosin staining revealed a reduction in the length of small intestinal crypts and the collapse of villi after burn injury, and these alterations were mitigated upon Gln supplementation (Figure 1b–e). These results indicate that Gln confers protection on the mucosal barrier in burned mice.

### Gln supplementation promoted crypt and IEC-6 cell proliferation while alleviating LPS-induced injury in intestinal organoids

ISCs located at the base of crypts serve as the fundamental mechanism for repairing damage to the intestinal mucosa [24]. We initially investigated the effect of Gln on ISCs and employed an antibody against the stem cell marker protein Lgr5 for stem-cell identification. We found reduced numbers of ISCs after burn injury, while supplementation with Gln significantly increased ISC abundance (Figure 2a). Subsequently, we investigated alterations in the proliferation of ISCs after burn injury and after Gln supplementation. Ki67 staining was predominantly localized to the crypt. Compared with that in the sham group, the proliferation of ISCs was decreased in the burned mice, while supplementation with Gln resulted in increased proliferation of ISCs (Figure 2b).

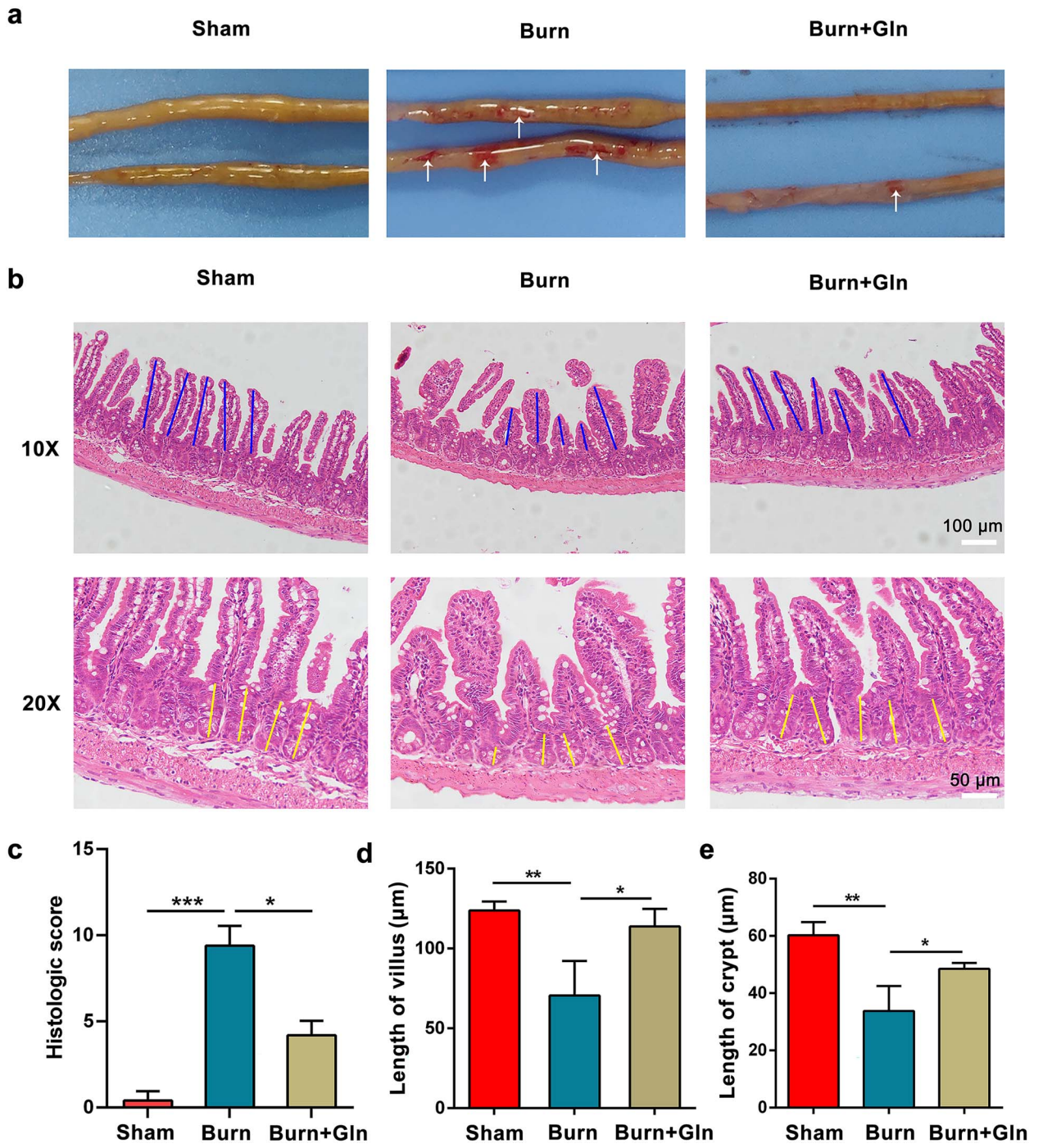


**Figure 1.** Gln mitigates burn-induced damage to the small intestine. (**a**) The surface of the small intestine is hemorrhagic after burn injury, and Gln supplementation can reduce hemorrhage on its surface. White arrows highlight surface congestion observed in the small intestine. (**b**) Representative images of pathological sections of the small intestine in different groups on Day 3 (Scale bar: 100 $\mu$m & 50 $\mu$m). (**c**) Histological injury score of the small intestine in each group. Lengths of small intestinal villi (**d**) and crypts (**e**) in mice from the sham, burn, and burn + Gln groups. Statistical analysis in (c) was performed using the Kruskal–Wallis test; data are presented as median with interquartile range. Statistical analyses in (d) and (e) were conducted using one-way ANOVA. Data are presented as mean ± SD; $^{*}p < 0.05$, $^{**}p < 0.01$, $^{***}p < 0.001$. *Gln* glutamine, *ANOVA* analysis of variance, *SD* standard deviation

These findings were further validated through RT-qPCR analysis (Figure 2c and d). The proliferation of ISCs can be inhibited by oxidative stress induced by burn injury. To assess the impact of varying Gln concentrations on cell growth, we used the CCK-8 assay to monitor changes in IEC-6 cell proliferation following treatment with different doses of Gln. Our findings revealed that optimal growth was observed at 2 and 4 mM glutamine (Figure S3, see online supplementary

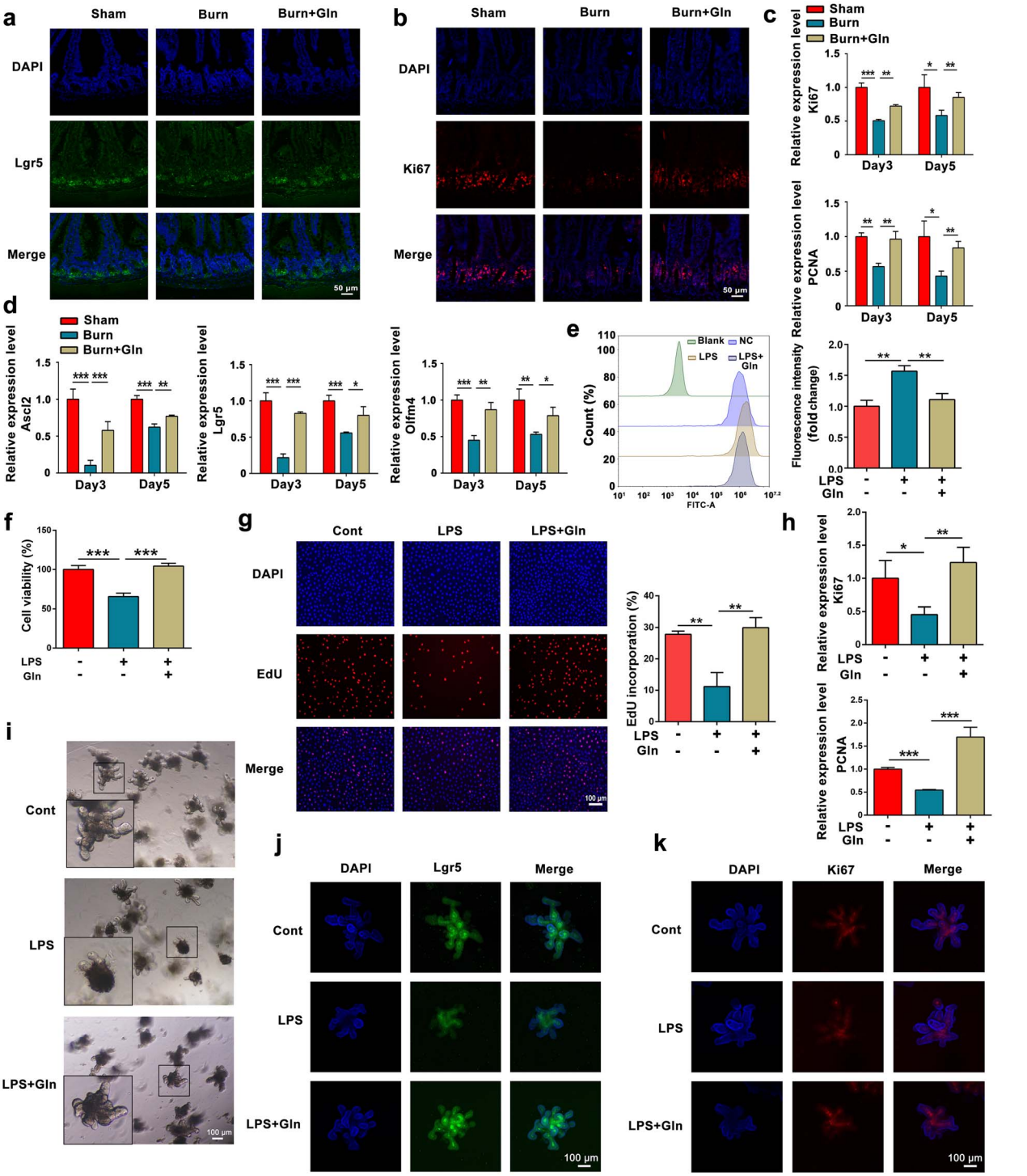


**Figure 2.** Gln supplementation promoted crypt and IEC6 cell proliferation. Immunofluorescence staining of pathological sections of the small intestinal samples from the sham, burn, and burn + Gln groups at 3 days post-burn injury using antibodies against (**a**) Lgr5 and (**b**) Ki67. Expression of (**c**) stemness-related and (**d**) proliferation-related genes after burn injury was assessed using RT–qPCR (Scale bar: 50 $\mu$m). (**e**) Concentration of ROS in IEC-6 cells was determined by flow cytometry using an H2DCFA probe. The cells were exposed to LPS (10 $\mu$g/ml) for 24 h and cultured in the absence or presence of 2 mM Gln. (**f**) CCK-8 and (**g**) EdU assays were used to determine the viability and proliferation of IEC-6 cells (Scale bar: 100 $\mu$m). Cells were exposed to LPS (10 $\mu$g/ml) for 24 h and cultured in the absence or presence of 2 mM Gln. (**h**) Expression of Ki67 and PCNA was quantified using RT–qPCR in IEC–6 cells cultured in the absence or presence of LPS (10 $\mu$g/ml, 24 h) or Gln (2 mM, 24 h). (**i**) Effects of LPS (10 $\mu$g/ml, 48 h) and Gln (2 mM, 48 h) on the growth of small intestinal organoids. Immunofluorescence staining was performed to analyze the proliferation of small intestinal organoids using antibodies against (**j**) Lgr5 and (**k**) Ki67 after culture in the absence or presence of 10 $\mu$g/ml LPS and 2 mM Gln for 48 h (Scale bar: 100 $\mu$m). Statistical analyses were conducted using one-way ANOVA. Data are presented as the mean ± SD; $^{*}p < 0.05$, $^{**}p < 0.01$, $^{***}p < 0.001$. *Cont* control, *SD* standard deviation, *DAPI* 4′,6-diamidino-2-phenylindole, *EdU* 5-Ethynyl-2′-deoxyuridine, *LPS* lipopolysaccharide, *Gln* glutamine, *CCK-8* cell counting kit-8, *RT–qPCR* real-time quantitative polymerase chain reaction, *IEC-6* intestine epithelial cell 6, *PCNA* proliferating cell nuclear antigen

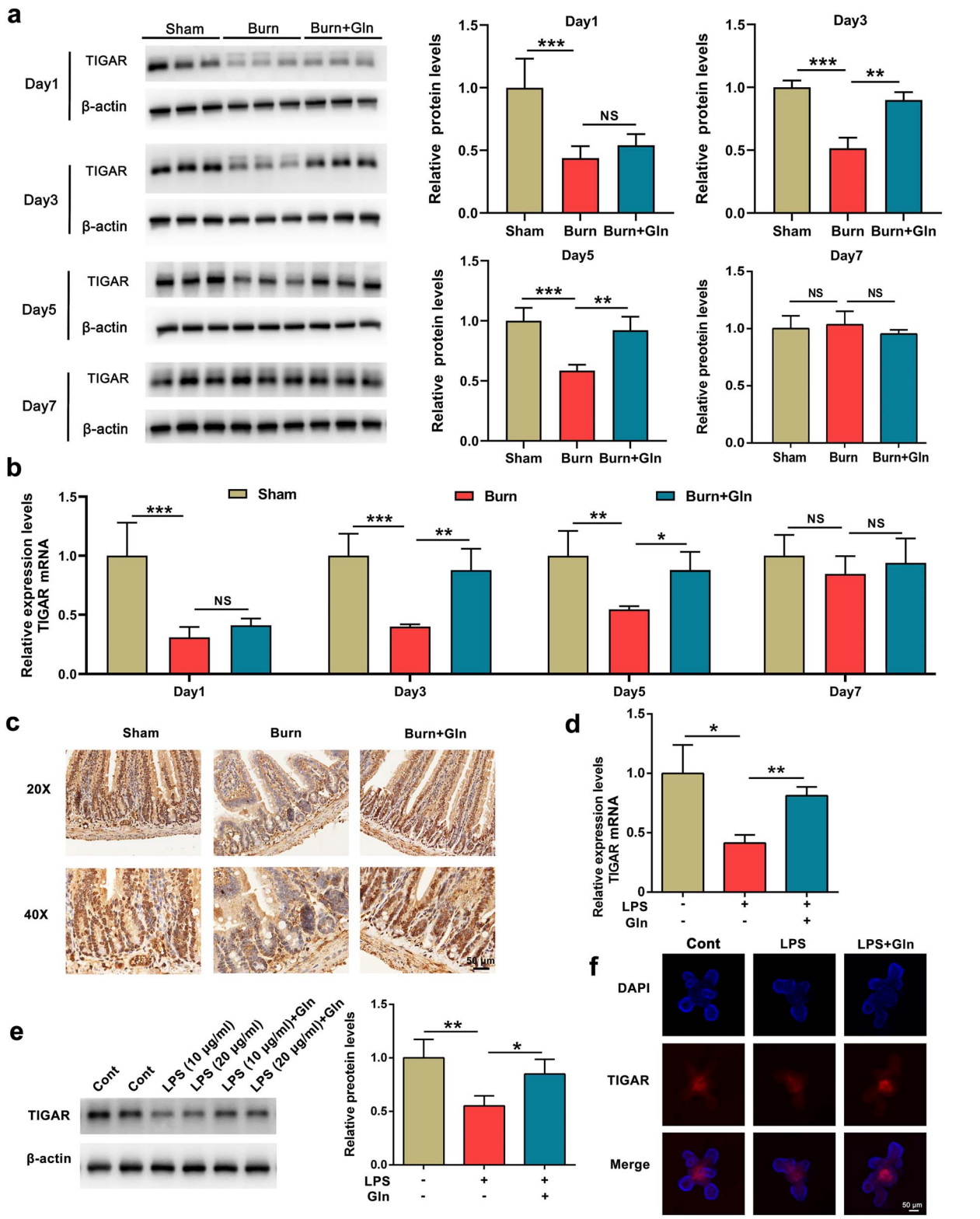


**Figure 3.** Gln promotes the expression of TIGAR after burn injury. (**a, b**) Expression of TIGAR protein and mRNA in the crypts of the intestine at 1, 3, 5, and 7 days post-injury in the sham, burn, and burn + Gln groups. Two-way repeated measures ANOVA revealed that Gln supply ($p < 0.001$) and time ($p < 0.001$) both had a statistically significant effect on TIGAR expression. There was statistically significant interaction between Gln supply and time ($p < 0.05$). (**c**) Immunohistochemical staining of intestinal sections using antibodies against TIGAR at 3 days post-injury (Scale bar: 50 $\mu$m). Expression of TIGAR mRNA and protein in IEC-6 cells treated with LPS (10 $\mu$g/ml) and Gln (2 mM) for 24 h was assessed by (**d**) RT–qPCR and (**e**) western blotting. Statistical analysis was conducted using one-way ANOVA. (**f**) Immunofluorescence staining was performed to analyze the changes in TIGAR in intestinal organoids (Scale bar: 50 $\mu$m). Data are presented as mean ± SD; $^{*}p < 0.05$, $^{**}p < 0.01$, $^{***}p < 0.001$. *NS* not significant, *SD* standard deviation, *DAPI* 4′,6-diamidino-2-phenylindole, *LPS* lipopolysaccharide, *Gln* glutamine, *RT–qPCR* real-time quantitative polymerase chain reaction, *Cont* control, *IEC-6* intestine epithelial cell 6, *TIGAR* TP53-induced glycolysis and apoptosis-regulator

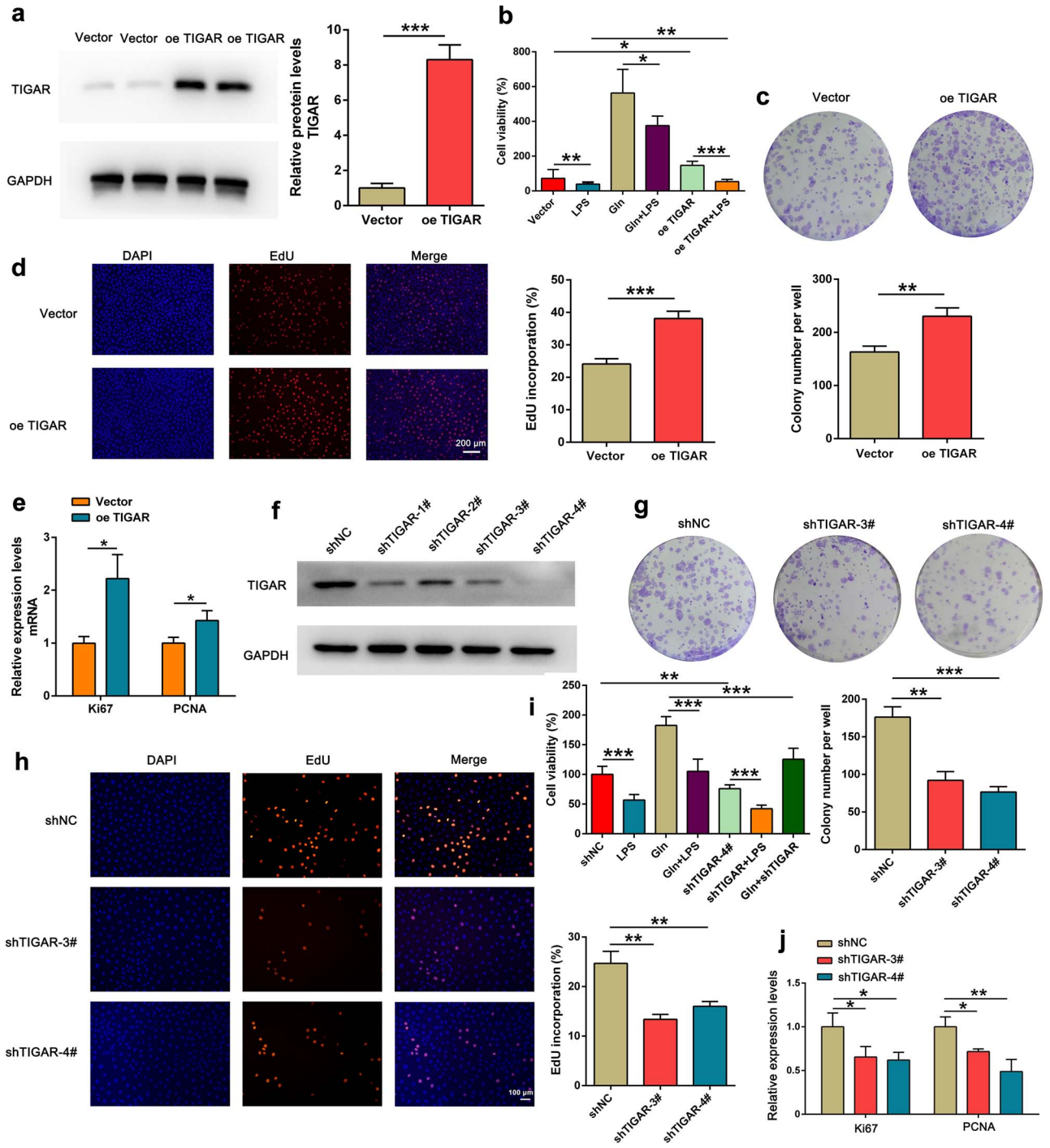


**Figure 4.** TIGAR facilitates the proliferation of IEC-6 cells. (**a**) Western blot analysis was performed to assess the expression of TIGAR in IEC-6 cells transfected with the indicated plasmid. (**b**) EdU, (**c**) colony formation and (**d**) CCK-8 assays were conducted in IEC-6 cells after overexpression (oe) of TIGAR (Scale bar: 200 $\mu$m). (**e**) Relative expression levels of Ki67 and PCNA in IEC-6 cells were assessed by RT–qPCR following TIGAR overexpression. (**f**) Knockdown efficiency was assessed by western blot analysis following transfection of four TIGAR siRNAs in IEC-6 cells. (**g**) Colony formation, (**h**) EdU, and (**i**) CCK-8 assays were used to investigate the proliferation of IEC-6 cells after TIGAR depletion (Scale bar: 100 $\mu$m). (**j**) Relative expression levels of Ki67 and PCNA in IEC-6 cells were assessed by RT–qPCR after TIGAR knockdown. Statistical analyses in (a, c, d and e) were performed using Student's t test; one-way ANOVA was used in others. Data are presented as mean ± SD; $^{*}p < 0.05$, $^{**}p < 0.01$, $^{***}p < 0.001$. *Cont* control, *DAPI* 4′,6-diamidino-2-phenylindole, *EdU* 5-Ethynyl-2′-deoxyuridine, *LPS* lipopolysaccharide, *Gln* glutamine, *CCK-8* cell counting kit-8, *RT–qPCR* real-time quantitative polymerase chain reaction, *IEC-6* intestine epithelial cell 6, *oe* over expression, *shNC* short hairpin negative control, *TIGAR* TP53-induced glycolysis and apoptosis-regulator, *PCNA* proliferating cell nuclear antigen, *GAPDH* glyceraldehyde-3-phosphate dehydrogenase, *SD* standard deviation

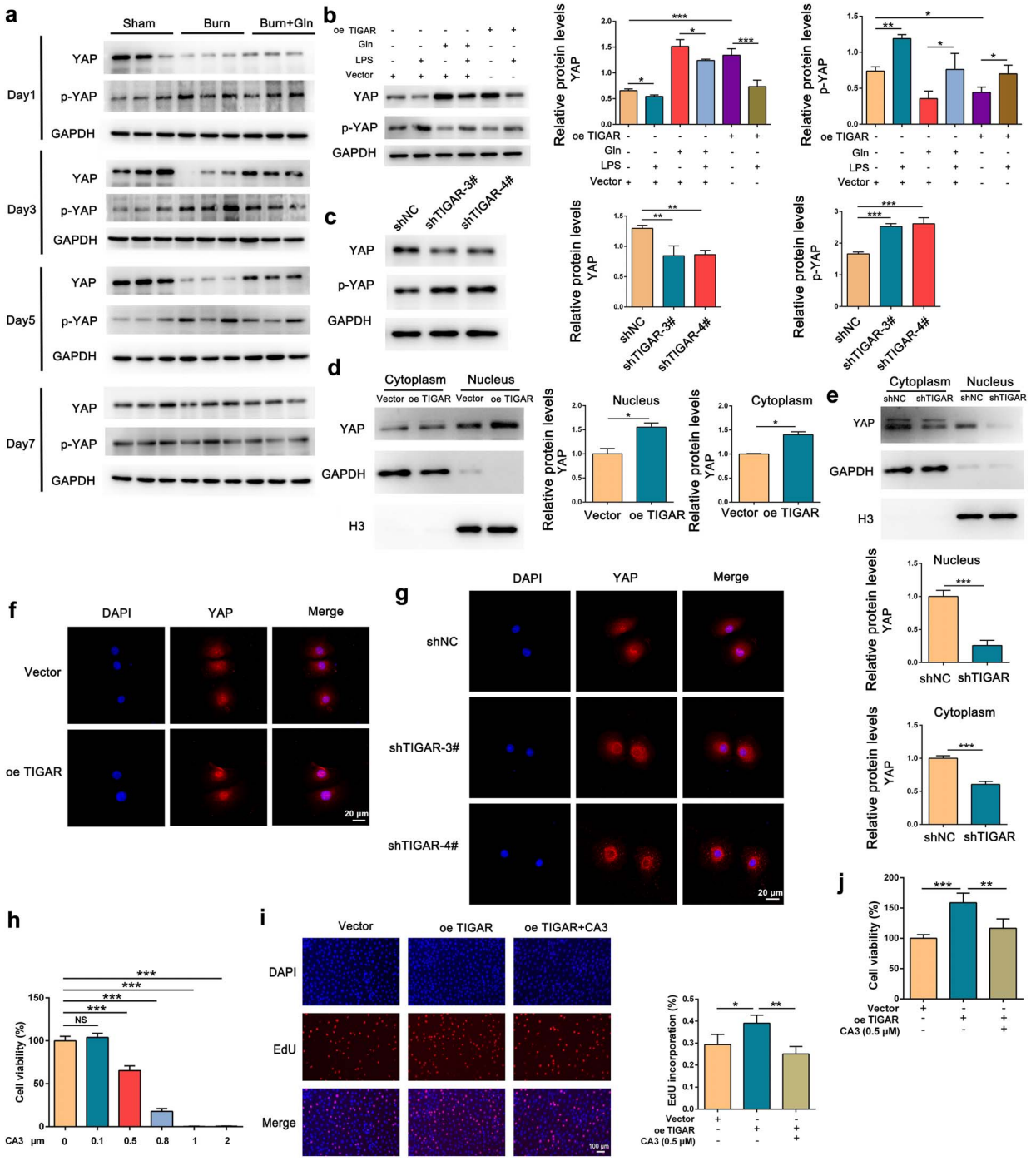


**Figure 5.** TIGAR promotes IEC-6 cell proliferation by facilitating the nuclear translocation of YAP. (**a**) Expression levels of YAP and p-YAP in intestinal crypts at 1, 3, 5, and 7 days were assessed by western blot analysis in the sham, burn, and burn + Gln groups. Changes in the expression of YAP and p-YAP in IEC-6 cells were assessed by western blot analysis following TIGAR overexpression (oe) (**b**) and knockdown (**c**), as well as LPS (10 $\mu$g/ml, 24 h) and Gln (2 mM, 24 h) treatment. Nuclear and cytoplasmic fractions of IEC-6 cells were isolated following TIGAR overexpression or knockdown, and the subcellular localization of YAP was assessed by (**d, e**) western blot and (**f, g**) immunofluorescence analyses (Scale bar: 20 $\mu$m). (**h**) IEC-6 cell viability was determined by CCK-8 assays after 24 h of treatment with different concentrations of the YAP inhibitor CA3. Proliferation of IEC-6 cells after TIGAR overexpression and treatment with CA3 (0.5 $\mu$M, 24 h) was evaluated using (**i**) EdU and (**j**) CCK-8 assays (Scale bar: 100 $\mu$m). Statistical analyses were conducted using one-way ANOVA, except in (d and e) where analyses were performed using Student's t test. Data are presented as mean ± SD; $^{*}p < 0.05$, $^{**}p < 0.01$, $^{***}p < 0.001$. *NS* not significant, *SD* standard deviation, *DAPI* 4′,6-diamidino-2-phenylindole, *LPS* lipopolysaccharide, *Gln* glutamine, *CCK-8* cell counting kit-8, *IEC-6* intestine epithelial cell 6, *oe* over expression, *shNC* short hairpin negative control, *TIGAR* TP53-induced glycolysis and apoptosis-regulator, *GAPDH* glyceraldehyde-3-phosphate dehydrogenase, *YAP* yes-associated protein, *H3* histone 3

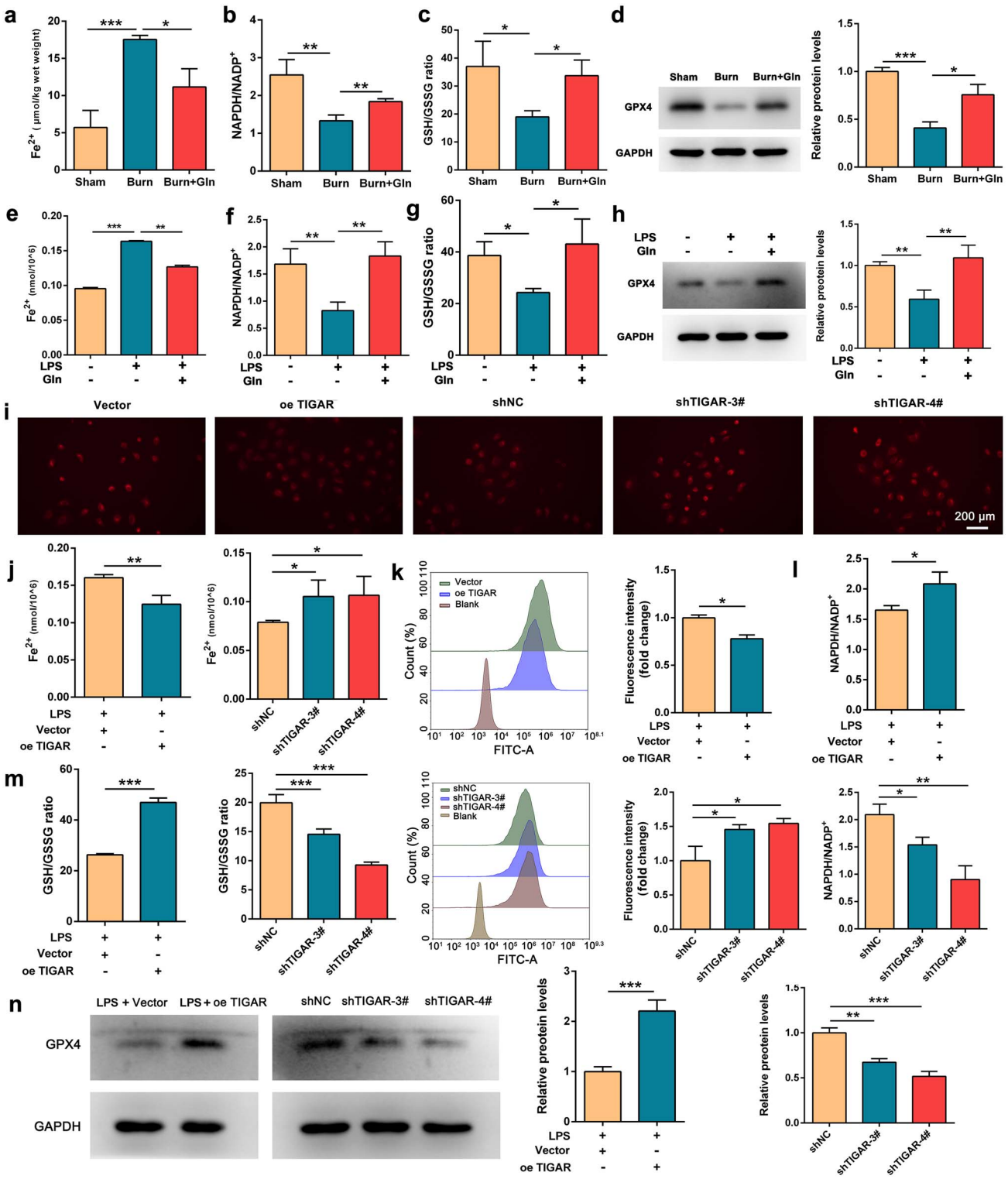


**Figure 6.** TIGAR inhibits ferroptosis in IEC-6 cells. (**a**) Concentration of $Fe^{2+}$, (**b**) NADPH/$NADP^{+}$ ratio and (**c**) GSH/GSSG ratio were determined in intestinal crypts from the sham, burn, and burn + Gln groups. (**d**) Western blot analysis was performed to investigate the expression of GPX4 in intestinal crypts from the sham, burn, and burn + Gln groups. (**e**) Concentration of $Fe^{2+}$, (**f**) NADPH/$NADP^{+}$ ratio, and (**g**) GSH/GSSG ratio were determined in IEC-6 cells following exposure to LPS (10 $\mu$g/ml, 24 h) and culture with Gln (2 mM, 24 h). (**h**) Expression of GPX4 in IEC-6 cells treated with LPS (10 $\mu$g/ml, 24 h) and Gln (2 mM, 24 h) was assessed by western blotting. Levels of $Fe^{2+}$ in IEC-6 cells after TIGAR overexpression (oe) and depletion were measured using (**i**) a Ferro Orange probe, and (**j**) a cell ferrous iron colorimetric assay kit (Scale bar: 200 $\mu$m). (**k**) Levels of ROS, (**l**) the NADPH/$NADP^{+}$ ratio, and (**m**) the GSH/GSSG ratio were assessed in IEC-6 cells after overexpression or knockdown of TIGAR. (**n**) Western blotting was used to determine the expression of GPX4 in TIGAR-overexpressing and TIGAR-knockdown IEC-6 cells. Statistical analyses were conducted using one-way ANOVA, except in overexpressing TIGAR, where analyses were performed using Student's t test. Data are presented as the means ± SD; $^{*}p < 0.05$, $^{**}p < 0.01$, $^{***}p < 0.001$. *LPS* lipopolysaccharide, *Gln* glutamine, *CCK-8* cell counting kit-8, *IEC-6* intestine epithelial cell 6, *oe* over expression, *shNC* short hairpin negative control, *GSH* glutathione, *GSSG* oxidized glutathione, *NADPH* nicotinamide adenine dinucleotide phosphate, *TIGAR* TP53-induced glycolysis and apoptosis-regulator, *GAPDH* glyceraldehyde-3-phosphate dehydrogenase, *GPX4* glutathione peroxidase 4, *SD* standard deviation

material), and subsequent cell experiments were conducted at a concentration of 2 mM. Intestinal bacterial translocation can lead to intestinal oxidative stress and inflammatory responses, which are also two important changes in the intestine after burn injury. To simulate inflammation and oxidative stress after burn injury, we treated IEC-6 cells with LPS, followed by the use of the H2DCFA probe for intracellular ROS detection. Subsequently, a significant increase in ROS levels was observed after LPS treatment, but ROS levels decreased in the Gln treatment group (Figure 2e). In addition, the viability and proliferation of IEC-6 cells were suppressed by LPS (Figure 2f and g), and the expression of proliferation-related genes decreased, whereas these effects were reversed upon Gln supplementation (Figure 2h).

Moreover, we investigated the effects of LPS or Gln on the growth of intestinal organoids. Compared with those in the control group, the organoids treated with LPS exhibited reduced sprouting, a more rounded shape, and disintegration. However, the addition of Gln effectively maintained the shape of the organoids (Figure 2i). Subsequently, immunofluorescence analysis revealed a decrease in $Lgr5^+$ cells (Figure 2j) and decreased proliferation after LPS treatment (Figure 2k). Notably, Gln supplementation promoted crypt organoid proliferation (Figure 2k). These data suggest that Gln inhibits oxidative stress, facilitates the proliferation of IEC-6 cells and ISCs, and preserves the functionality of intestinal organoids.

### Gln promotes the proliferation of crypt and IEC-6 cells by upregulating the expression of TIGAR

TIGAR functions as a glycolytic inhibitory enzyme, facilitating the diversion of glucose from the glycolytic pathway to the PPP, thereby increasing NADPH production [25]. We hypothesized that Gln promotes NADPH synthesis by modulating TIGAR expression. Initially, we assessed alterations in TIGAR levels within small intestinal crypts after burn injury. Two-way repeated measures ANOVA revealed that Gln supply ($P < 0.001$) and time ($P < 0.01$) both had a statistically significant effect on TIGAR expression. There was statistically significant interaction between Gln supply and time ($P < 0.05$). The results revealed a significant decrease in both TIGAR mRNA and protein levels 1 to 5 days post-burn injury. The decline on the first day after burn injury was the most significant. Subsequently, a gradual recovery was observed, and the values almost recovered to the baseline at 7 days post-burn injury. Notably, Gln supplementation did not affect TIGAR expression immediately on Day 1, but this treatment significantly upregulated TIGAR expression on Day 3 after burn injury (Figure 3a and b). Therefore, subsequently, experimental samples were collected on the third day after burn injury. The immunohistochemical results also demonstrated a marked reduction in TIGAR expression on the third day post-burn injury, and the expression was subsequently restored by Gln treatment (Figure 3c). Moreover, TIGAR exhibited predominant localization within ISCs (Figure 3c). Similarly, the protein and mRNA expression of TIGAR decreased in IEC-6 cells and organoids upon treatment with LPS, whereas supplementation with Gln restored the levels of TIGAR (Figure 3d–f).

To investigate the impact of TIGAR on cellular proliferation, we generated TIGAR overexpression constructs and four shRNA plasmids. Western blot analysis revealed a significant upregulation of TIGAR protein upon overexpression (Figure 4a). CCK-8, colony formation, and EdU assays indicated that the overexpression of TIGAR promoted the proliferation of IEC-6 cells (Figure 4b–d) and that TIGAR promoted the expression of proliferation-related genes (Figure 4e). All four shRNAs had significant effects on the TIGAR protein level (Figure 4f). Among them, shTIGAR-3# and shTIGAR-4# were chosen for subsequent experimental investigations. Knockdown of TIGAR attenuated cell proliferation in IEC-6 cells cultured with Gln (Figure 4g–i) and decreased the expression of Ki67 and PCNA (Figure 4j). These results indicate that Gln promotes the proliferation of crypt and IEC-6 cells by upregulating TIGAR expression.

### TIGAR facilitates the nuclear translocation of YAP and promotes IEC-6 cell proliferation

In previous studies, we demonstrated that Gln effectively increases the proliferation of ISCs by inhibiting the phosphorylation of YAP [26]. TIGAR acts as a phosphatase that can facilitate protein dephosphorylation [25,27]. Therefore, we postulated that TIGAR may increase cellular proliferation through the inhibition of YAP phosphorylation. The fluctuation of total YAP protein exhibited a parallel trend with TIGAR, showing a significant reduction on Day 3, and the expression was not restored by Gln supplementation (Figure 5a). Conversely, p-YAP demonstrated a notable increase on Day 3 but decreased upon Gln intervention (Figure 5a). After the treatment of IEC-6 cells with LPS, the protein level of YAP decreased, while the p-YAP level increased, a trend that was reversed by Gln supplementation (Figure 5b). Overexpression of TIGAR resulted in an increase in YAP expression and a decrease in p-YAP levels (Figure 5b), while the opposite effect occurred when TIGAR was knocked down (Figure 5c). YAP can translocate into the nucleus to control the transcription of target genes. The nuclear translocation of YAP is associated with its phosphorylation. p-YAP is degraded in the cytoplasm, while non-phosphorylated YAP can successfully enter the nucleus [28]. Subsequently, we investigated the impact of TIGAR on YAP nuclear localization and the expression of proliferation-related genes. The results revealed that overexpression of TIGAR led to an increase in nuclear YAP levels (Figure 5d and f), whereas knockdown of TIGAR resulted in a decrease in nuclear YAP levels (Figure 5e and g). Furthermore, CA3 inhibited YAP activity [29] subsequent to TIGAR overexpression, which resulted in reduced cell proliferation, as evidenced by CCK-8 and EdU assays (Figure 5h–j). Consistently, our findings support the notion that TIGAR facilitates YAP activation, leading to its nuclear translocation and promotion of IEC-6 cell proliferation.

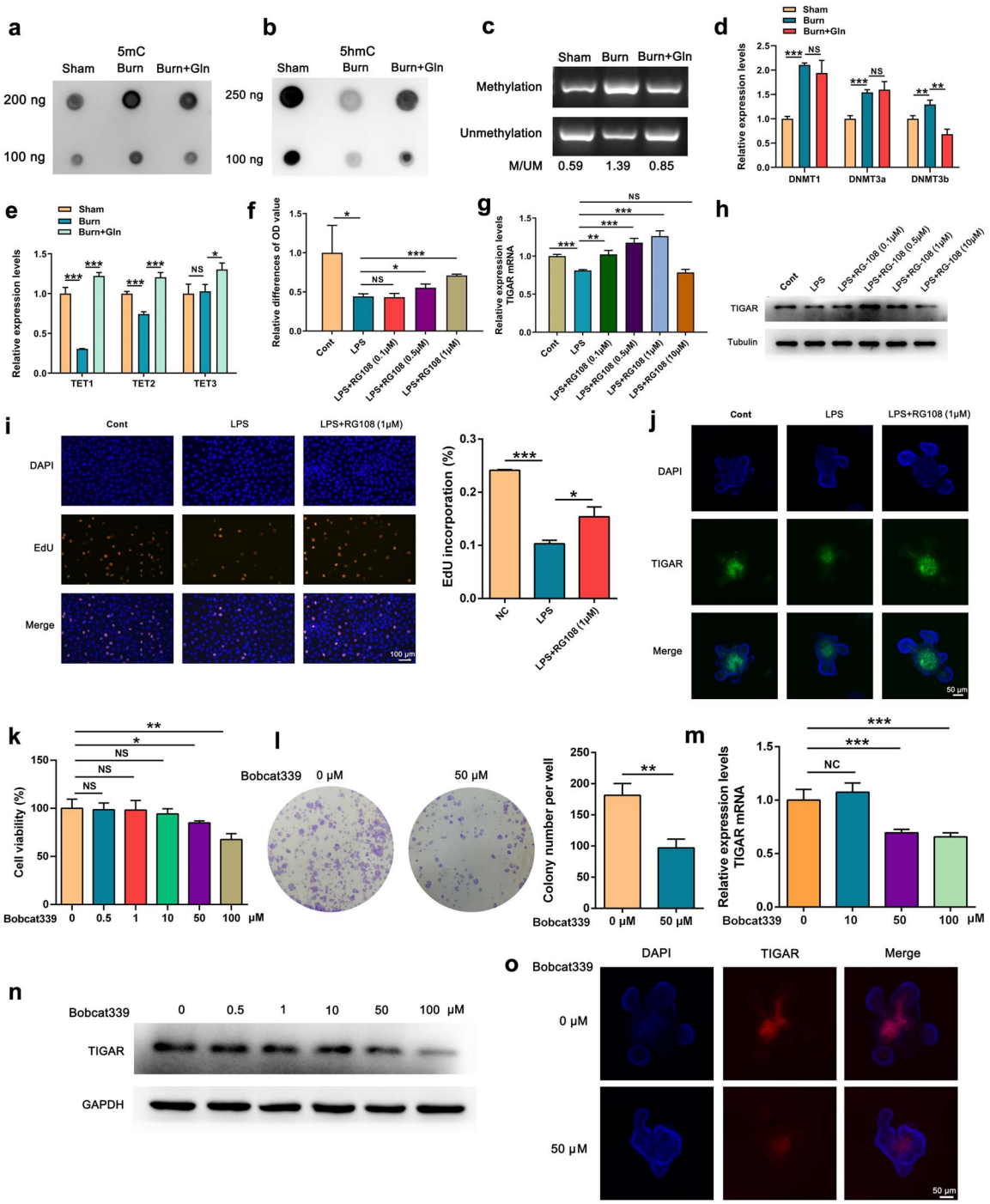


**Figure 7**. Glutamine promotes the proliferation of IEC-6 cells by inhibiting TIGAR promoter methylation. (**a, b**) Levels of 5mC and 5hmC in the crypt cells of sham, burn, and burn + Gln groups of mice 3 days after burn injury were assessed using dot blot analysis. (**c**) Methylation/unmethylation ratio in the crypt cells of the sham, burn and burn + Gln groups of mice at 3 days post-burn injury was determined by methylation-specific PCR. Expression of (**d**) DNMTs and (**e**) TETs in intestinal crypts was investigated by RT–qPCR. (**f**) IEC-6 cell viability was assessed by CCK-8 assays following treatment with different concentrations of the DNMT inhibitor RG108. (**g, h**) mRNA and protein expression of TIGAR was determined using RT-qPCR and western blotting following a 24 h incubation with LPS (10 $\mu$g/ml) and RG108 (0.5 $\mu$M). (**i**) EdU assay was used to evaluate the proliferation of IEC-6 cells treated with LPS (10 $\mu$g/ml) and RG108 (0.5 $\mu$M) for 24 h. (**j**) Immunofluorescence was performed to assess the level of TIGAR in the intestinal organoids treated with LPS (10 $\mu$g/ml) and RG108 (0.5 $\mu$M) for 48 h. (**k**) CCK-8 assay was used to determine IEC-6 cell viability after treatment with different concentrations of the TET inhibitor Bobcat339 for 24 h. (**l**) Colony formation assays were conducted in IEC-6 cells treated with 50 $\mu$M Bobcat339. (**m, n**) RT-qPCR and western blotting were used to assess the levels of TIGAR mRNA and protein in IEC-6 cells cultured with different concentrations of Bobcat339. (**o**) Level of TIGAR in the organoids treated with 50 $\mu$M Bobcat339 for 24 h was analyzed by immunofluorescence. Statistical analyses were conducted using one-way ANOVA, except in (l) where analysis was performed using Student's t test. Data are presented as mean ± SD, $^{*}p < 0.05$, $^{**}p < 0.01$, $^{***}p < 0.001$. *NS* not significant, *DAPI* 4′,6-diamidino-2-phenylindole, *EdU* 5-Ethynyl-2′-deoxyuridine, *LPS* lipopolysaccharide, *Gln* glutamine, *CCK-8* cell counting kit-8, *IEC-6* intestine epithelial cell 6, *oe* over expression, *shNC* short hairpin negative control, *Cont* control, *5mC* 5-methylcytosine, *5hmC* 5-hydroxymethylcytosine, *TIGAR* TP53-induced glycolysis and apoptosis-regulator, *GAPDH* glyceraldehyde-3-phosphate dehydrogenase, *TET* ten-eleven translocation, *DNMT* DNA methyltransferase, *SD* standard deviation

### TIGAR mitigated LPS-induced ferroptosis in IEC-6 cells

Oxidative stress after burn injury induces cellular lipid peroxidation, leading to ferroptosis, while excessive ROS deplete GSH, resulting in diminished activity of GPX4, a key regulatory enzyme in the antioxidant system, thereby exacerbating ferroptosis [30]. We investigated the alterations in $Fe^{2+}$ levels within the small intestinal crypts of mice after burn injury. Compared with those in the sham group, $Fe^{2+}$ levels were elevated post-burn injury, accompanied by a decrease in NADPH and GSH synthesis. However, supplementation with Gln resulted in a reduction in $Fe^{2+}$ levels and an increase in NADPH and GSH synthesis (Figure 6a–c). Additionally, western blot analysis revealed a decrease in GPX4 expression after burn injury, which could be reversed by Gln supplementation (Figure 6d). The same effect was observed in the IEC-6 cells treated with LPS and Gln (Figure 6e–h). Following TIGAR overexpression in the LPS-treated IEC-6 cells, NADPH and GSH contents and GPX4 protein expression increased, while $Fe^{2+}$ and ROS levels decreased. Conversely, TIGAR knockdown had the opposite effect (Figure 6i–n). These findings suggest that TIGAR mitigates LPS-induced ferroptosis in IEC-6 cells.

### Gln promotes the proliferation of intestinal stem cells and IEC-6 cells by inhibiting TIGAR promoter methylation

The accumulation of ROS can impact the regulation of gene promoter methylation and subsequent gene expression as a consequence of ROS-mediated modulation of methylase activity [31]. Methylase DNA methyltransferases (DNMTs) catalyze substitution of the 5′ hydrogen on the dinucleotide cytosine ring on the cytosine-phosphate-guanine island to generate 5mC, which causes DNA methylation and inhibits gene transcription [32]. The demethylase ten-eleven translocations (TETs) oxidize 5mC in the DNA sequence to 5hmC, 5-formylcytosine and 5-carboxylcytosine. Eventually, 5-carboxylcytosine is selectively recognized by thymine-DNA glycosylase and is reversed to unmodified cytosine by base resection repair [33]. Given the reduction in TIGAR expression under conditions of oxidative stress, we hypothesized that burn injury increases methylation of the TIGAR gene promoter, while Gln can mitigate TIGAR promoter methylation and promote its expression by modulating methylase or demethylase activity.

We quantified the levels of total 5mC and 5hmC in the small intestinal crypt after burn injury. DNA dot blot analysis revealed an increase in DNA methylation and a decrease in demethylation within the small intestinal crypts of mice post-burn injury, whereas the administration of Gln reversed these changes (Figure 7a and b). The methylation of TIGAR in small intestinal crypts was found to be increased, while Gln supplementation had the opposite effect, as demonstrated by the methylation-specific PCR assay (Figure 7c). In addition, we observed an increase in DNMT1, DNMT3a, and DNMT3b expression, while TET1 and TET2 expression decreased after burn injury (Figure 7d and e). Following Gln supplementation, there was no significant change in DNMT1 or DNMT3a expression, but there was a decrease in DNMT3b expression, whereas TET1 and TET2 expression was upregulated (Figure 7d and e). The inhibition of DNMT3b activity in IEC-6 cells and organoids cultured without Gln by a low concentration of RG108 resulted in the upregulation of TIGAR expression (Figure 7g and h) and increased cell viability compared to that in the LPS group (Figure 7f and i). The inhibition of TET1/2 activity by Bobcat339 in IEC-6 cells and organoids cultured with Gln led to a decrease in cell viability (Figure 7k and l) and a reduction in TIGAR expression (Figure 7m–o). These results suggest that Gln plays an important role in the regulation of TIGAR promoter methylation by inhibiting DNMT3b and promoting TET1/2.

## Discussion

Oxidative stress induced by burn injury not only causes damage to intestinal epithelial cells and increases intestinal mucosal permeability but also impedes the proliferation of ISCs, thereby resulting in delayed repair of damaged intestinal mucosa [34]. How to regulate the function of ISCs and accelerate the repair of damaged tissues is a common concern in both basic and clinical medicine. In this study, we observed an increase in ROS levels in the ISCs of mice after burn injury. Concurrently, TIGAR synthesis decreased, which led to reduced NADPH levels and subsequent inhibition of cell proliferation. However, upon administration of Gln, the proliferative activity of stem cells and the regenerative capacity of the intestinal mucosa were significantly increased. Mechanistic research on intestinal organoids and IEC-6 inflammatory cell models has demonstrated that Gln can effectively inhibit the methylation of the TIGAR promoter, thereby promoting TIGAR expression, accelerating NADPH synthesis, suppressing ferroptosis, and reversing the inhibition of proliferation induced by oxidative stress, thereby leading to a reduction in intestinal mucosal damage and facilitating tissue repair.

Ischemia–reperfusion plays a pivotal role in the pathogenesis of multiple-organ or tissue damage after burn injuries. Upon reperfusion, activation of the xanthine oxidase system leads to a substantial increase in cytoplasmic ROS levels [35,36]. Additionally, burn-induced damage to cellular mitochondria leads to the leakage of electrons at the terminal end of the mitochondrial membrane's respiratory chain, facilitating the generation of ROS by ubiquinone oxidoreductase (Complex 1) [37]. Excessive ROS not only induce lipid peroxidation in the plasma membrane, leading to structural damage and impairment of cellular integrity, but also initiate iron ion aggregation, resulting in cellular ferroptosis [38]. In this study, there was a significant increase in ROS levels in the ISCs of mice after burn injury, leading to excessive depletion of GSH and a substantial decrease in its content. Concurrently, the synthesis of NADPH, which facilitates the conversion of GSSG into GSH, was significantly decreased. Consequently, impaired ROS clearance and disrupted redox

balance occur within cells, ultimately resulting in $Fe^{2+}$ accumulation and ferroptosis. The glucose PPP is the main pathway of NADPH synthesis *in vivo*, accounting for >60% of the total NADPH [39]. TIGAR is a key regulator in the control of NADPH synthesis, facilitating the diversion of glucose from the glycolytic pathway to the PPP pathway, thereby significantly amplifying NADPH production [40]. Gln can facilitate the synthesis of NADPH and GSH, thereby inhibiting ferroptosis [41]. Similarly, TIGAR also promotes the synthesis of NADPH and GSH to counteract ferroptosis [42]. Based on evidence that Gln can promote the PPP by activating G6PD [19], Gln likely increases the production of NADPH and GSH to prevent ferroptosis by regulating TIGAR. In this study, we observed a significant reduction in ISC TIGAR synthesis post-burn injury, which was closely associated with a decrease in NADPH levels and an increase in ferroptosis. To elucidate the relationship between TIGAR and ferroptosis, we manipulated its expression. Following TIGAR overexpression, a decrease in the concentration of $Fe^{2+}$ was observed in IEC-6 cells, resulting in the inhibition of ferroptosis. Conversely, knockdown of TIGAR had the opposite effects, indicating that TIGAR can impede $Fe^{2+}$ accumulation and suppress ferroptosis.

Further studies showed that TIGAR can also promote ISC proliferation by affecting the Hippo–YAP signaling pathway, a pivotal regulatory pathway for stem cell proliferation [43]. As the principal effector protein within this signaling cascade, YAP is extensively implicated in orchestrating cellular processes such as proliferation, differentiation, apoptosis and senescence [44]. YAP is a transcriptional coactivator that needs to be transported from the cytoplasm to the nucleus and subsequently bind to TEAD or other transcription factors within the nucleus to regulate target-gene expression [45]. Upon phosphorylation, the nuclear membrane translocation of YAP is impeded, resulting in loss of its proliferative activity [46]. TIGAR was reported to exhibit phosphatase activity and mediate the dephosphorylation of multiple proteins to modulate their functional regulation [47]. In this study, overexpression of TIGAR led to a significant reduction in the phosphorylation level of the YAP protein, while knockdown of TIGAR resulted in a substantial increase in phosphorylation. These findings provide compelling evidence for the inhibitory effect of TIGAR on YAP phosphorylation and its crucial involvement in maintaining stem cell proliferation. The suppression of TIGAR synthesis after burn injury leads to diminished NADPH production, disruption of the GSH/GSSG balance and attenuation of cellular antioxidant capacity. Additionally, this change results in increased YAP phosphorylation levels, which inhibits cell proliferation. Therefore, TIGAR can mitigate ISC damage, facilitate cellular proliferation, and expedite the restoration of impaired mucosa through the maintenance of the cellular redox balance and promotion of cell proliferation.

In this study, we observed a significant initial decrease in TIGAR levels in ISCs post-burn injury, followed by a gradual increase. The levels were basically the same as those before the injury at 7 days post-burn injury. This change was closely associated with alterations in glucose metabolic patterns after burn injury. To meet the immediate energy demand during the early stages of burns, glycolysis plays a predominant role as the primary mode of energy supply [48]. In this period, a low level of TIGAR is advantageous for rapid glucose oxidation for energy generation via glycolysis. However, a decrease in TIGAR persistence can lead to a sustained increase in glycolytic activity, hindering the efficient utilization of glucose and resulting in cellular damage due to lactic acid accumulation [49]. Moreover, prolonged inhibition of the PPP leads to a reduction in NADPH production, which hampers the maintenance of the cellular redox balance. Although Gln administration did not alter the overall trend of TIGAR, it significantly mitigated the decrease in TIGAR levels. Notably, on the third day post-injury, TIGAR levels increased more than 2-fold and approached preinjury levels under Gln treatment. This finding suggests that Gln promotes the substantial synthesis of TIGAR in cells, facilitating the diversion of excessive glucose from glycolysis to the PPP. Our previous study revealed that Gln increased NADPH synthesis by promoting the glycosylation of G6PD, a pivotal enzyme in the PPP [19]. In this study, we confirmed that Gln redirects glucose from glycolysis to the PPP through TIGAR regulation. Additionally, Gln promotes NADPH synthesis by increasing the flow of glucose toward the PPP and increasing the activity of the key enzyme G6PD in this pathway. These findings undoubtedly deepen our understanding of how Gln maintains the cellular redox balance.

In recent years, increasing attention has been devoted to elucidating the regulatory role of Gln in cellular metabolism. This role encompasses its involvement in metabolic reprogramming of the tricarboxylic acid cycle [50], regulation of the urea cycle, and redox homeostasis [51], as well as its contribution to DNA methylation [52]. Further investigations revealed that the increase in methylation at the TIGAR promoter in ISCs after burn injury is a pivotal factor impeding TIGAR synthesis. This process is intricately associated with the intracellular accumulation of ROS postburn. Previous reports have shown that cellular oxidative stress can induce the activation of methylase DNMTs [53] and inhibit demethylase TETs [54], thereby augmenting promoter methylations in various genes. In both animal and cell models, we observed that an increase in ROS is a crucial factor in promoting TIGAR promoter methylation, while the administration of Gln leads to a reduction in intracellular ROS levels, thereby attenuating the extent of methylation. Notably, Gln promoted the expression of the demethylase TET1/2, thereby accelerating TIGAR expression. However, this effect diminished significantly upon administration of the TET inhibitor Bobcat339. This observation strongly suggested that Gln plays a crucial role in reducing the methylation level of the TIGAR promoter by activating TET1/2, thus facilitating the synthesis of TIGAR. We also found that TIGAR expression

increased after RG108 was administered to inhibit DNMTs in LPS-treated cells, while Gln had an inhibitory effect on the methylase Dnmt3b. Therefore, we believe that Gln exerts its effects by inhibiting methylase activity and activating demethylase, leading to a reduction in the methylation of the TIGAR promoter, promoting TIGAR synthesis, mitigating ferroptosis, and facilitating the proliferation of ISCs post-burn injury, ultimately facilitating the repair of damaged intestinal mucosa. However, the exact mechanism by which Gln inhibits methylation, especially the regulation of TET1/2 and Dnmt3b activity, remains incompletely understood. This is the key issue that we will focus on in our future research.

## Conclusions

In this study, we investigated the molecular mechanism underlying the Gln-mediated promotion of TIGAR expression and the alleviation of intestinal mucosal barrier damage, with a specific focus on its role in regulating oxidative stress. We report two principal findings. First, TIGAR promotes the proliferation of ISCs by facilitating YAP nuclear translocation, and protects against ferroptosis by increasing the synthesis of NADPH and GSH. Second, we found that Gln stimulates ISC proliferation by inhibiting TIGAR promoter methylation through Dnmt3b suppression and by increasing TET1/2 expression. These discoveries increase our understanding of the regulatory role of Gln in cell metabolism and may inform the therapeutic use of Gln in the context of burns.

## Abbreviations

ANOVA: Analysis of variance; DMEM: Dulbecco's modified Eagle's medium; DNMT: DNA methyltransferase; FITC: Fluorescein isothiocyanate-dextran; Gln: Glutamine; GPX4: Glutathione peroxidase 4; GSH: Glutathione; GSSG: Glutathione disulfide; G6PD: Glucose-6-phosphate dehydrogenase; IEC-6, Intestinal epithelial cell line 6; ISCs: Intestinal stem cells; Lgr5: Leucine-rich repeat-containing G protein-coupled receptor 5; LPS: Lipopolysaccharide; 5hmC: 5-Hydroxymethylcytosine; 5mC: 5-Methylcytosine; NADPH: Nicotinamide adenine dinucleotide phosphate; PBS: Phosphate-buffered saline; PCNA: Proliferating cell nuclear antigen; PPP: Pentose phosphate pathway; ROS: Reactive oxygen species; RT-qPCR: Real-time quantitative polymerase chain reaction; shRNA: Short hairpin RNA; TET: Ten-eleven translocation; TIGAR: TP53-induced glycolysis and apoptosis regulator; YAP: Yes-associated protein.

## Author contributions

Panyang Zhang (Conceptualization [supporting], Methodology [equal], Resources [lead], Software [lead], Validation [lead], Visualization [lead], Writing—original draft [lead], Dan Wu (Validation [supporting]), Xule Zha (Methodology [supporting], Software [supporting]), Sen Su (Methodology [supporting], Software [supporting]), Yajuan Zhang (Validation [supporting]), Yan Wei (Validation [supporting]), Lin Xia (Validation [supporting]), Shijun Fan (Validation [supporting]), and Xi Peng (Conceptualization [lead], Data curation [equal], Formal analysis [equal], Funding acquisition [lead], Project administration [lead], Supervision [lead], Writing—review & editing [lead]).

## Supplementary data

Supplementary data is available at *Burns & Trauma* online.

## Ethics approval and consent to participate

Animal experiments were approved by the Animal Ethics Committee of Southwest Hospital, Third Military Medical University and performed in accordance with the national guidelines for animal welfare (No. AMUWEC20210636).

## Conflict of interest

All authors declare that they have no competing interests.

## Funding

This research was funded by the National Natural Science Foundation of China (No. 82172202), the Natural Science Foundation of Chongqing, China (CSTB2024NSCQ-MSX0454) and the Innovative Leading Talents Project of Chongqing, China (No. cstc2022ycjh-bgzxm0148).

## References

1. Knuth CM, Auger C, Jeschke MG. Burn-induced hypermetabolism and skeletal muscle dysfunction. *Am J Physiol Cell Physiol* 2021;321:C58–c71. https://doi.org/10.1152/ajpcell.00106.2021.
2. Huang J, Chen Y, Guo Z, Yu Y, Zhang Y, Li P, *et al*. Prospective study and validation of early warning marker discovery based on integrating multi-omics analysis in severe burn patients with sepsis. *Burns Trauma* 2023;11:tkac050. https://doi.org/10.1093/burnst/tkac050.
3. Zha X, Su S, Wu D, Zhang P, Wei Y, Fan S, *et al*. The impact of gut microbiota changes on the intestinal mucus barrier in burned mice: a study using 16S rRNA and metagenomic sequencing. *Burns Trauma* 2023;11:tkad056. https://doi.org/10.1093/burnst/tkad056.
4. Qin C, Jiang Y, Chen X, Bian Y, Wang Y, Xie K, *et al*. Dexmedetomidine protects against burn-induced intestinal barrier injury via the MLCK/p-MLC signalling pathway. *Burns J Int Soc Burn Inj* 2021;47:1576–85. https://doi.org/10.1016/j.burns.2021.01.017.
5. Luo H, Li M, Wang F, Yang Y, Wang Q, Zhao Y, *et al*. The role of intestinal stem cell within gut homeostasis: focusing on its interplay with gut microbiota and the regulating pathways. *Int J Biol Sci* 2022;18:5185–206. https://doi.org/10.7150/ijbs.72600.
6. Beckmann N, Pugh AM, Caldwell CC. Burn injury alters the intestinal microbiome's taxonomic composition and functional gene expression. *PLoS One* 2018;13:e0205307. https://doi.org/10.1371/journal.pone.0205307.
7. Xi P, Hui TL, Yi YZ, Pei W, Liang WS. Relationship between enterogenous hypermetabolism and intestine injury after severe burn injury. *Acta Acade Med Militaris Tertiae* 2003;25:1745–7.

8. Pentinmikko N, Katajisto P. The role of stem cell niche in intestinal aging. *Mech Ageing Dev* 2020;191:111330. https://doi.org/10.1016/j.mad.2020.111330.
9. Sphyris N, Hodder MC, Sansom OJ. Subversion of niche-signalling pathways in colorectal cancer: what makes and breaks the intestinal stem cell. *Cancers* 2021;13:1000. https://doi.org/10.3390/cancers13051000.
10. Nath A, Chakrabarti P, Sen S, Barui A. Reactive oxygen species in modulating intestinal stem cell dynamics and function. *Stem Cell Rev Rep* 2022;18:2328–50. https://doi.org/10.1007/s12015-022-10377-1.
11. Wang D, Li P, Odle J, Lin X, Zhao J, Xiao K, *et al.* Modulation of intestinal stem cell homeostasis by nutrients: a novel therapeutic option for intestinal diseases. *Nutr Res Rev* 2022;35:150–8. https://doi.org/10.1017/S0954422421000172.
12. Morris O, Jasper H. Reactive oxygen species in intestinal stem cell metabolism, fate and function. *Free Radic Biol Med* 2021;166:140–6. https://doi.org/10.1016/j.freeradbiomed.2021.02.015.
13. Chen Y, Tsai YH, Tseng BJ, Tseng SH. Influence of growth hormone and glutamine on intestinal stem cells: a narrative review. *Nutrients* 2019;11:1941. https://doi.org/10.3390/nu11081941.
14. Ma N, Chen X, Liu C, Sun Y, Johnston LJ, Ma X. Dietary nutrition regulates intestinal stem cell homeostasis. *Crit Rev Food Sci Nutr* 2022;63:11263–74. https://doi.org/10.1080/10408398.2022.2087052.
15. Amirato GR, Borges JO, Marques DL, Santos JMB, Santos CAF, Andrade MS, *et al.* L-glutamine supplementation enhances strength and power of knee muscles and improves Glycemia control and plasma redox balance in exercising elderly women. *Nutrients* 2021;13:1025. https://doi.org/10.3390/nu13031025.
16. Wischmeyer PE. Glutamine in burn injury. *Nutr Clin Prac* 2019;34:681–7. https://doi.org/10.1002/ncp.10362.
17. Xiao Q, Chen YH, Pratama SA, Chen YL, Shirakawa H, Peng HC, *et al.* The prophylactic effects of glutamine on muscle protein synthesis and degradation in rats with ethanol-induced liver damage. *Nutrients* 2021;13:2788. https://doi.org/10.3390/nu13082788.
18. DeBerardinis RJ, Cheng T. Q's next: the diverse functions of glutamine in metabolism, cell biology and cancer. *Oncogene* 2010;29:313–24. https://doi.org/10.1038/onc.2009.358.
19. Wu D, Su S, Zha X, Wei Y, Yang G, Huang Q, *et al.* Glutamine promotes O-GlcNAcylation of G6PD and inhibits AGR2 S-glutathionylation to maintain the intestinal mucus barrier in burned septic mice. *Redox Biol* 2023;59:102581. https://doi.org/10.1016/j.redox.2022.102581.
20. Bensaad K, Tsuruta A, Selak MA, Vidal MN, Nakano K, Bartrons R, *et al.* TIGAR, a p53-inducible regulator of glycolysis and apoptosis. *Cell* 2006;126:107–20. https://doi.org/10.1016/j.cell.2006.05.036.
21. Paneque A, Fortus H, Zheng J, Werlen G, Jacinto E. The Hexosamine biosynthesis pathway: regulation and function. *Genes* 2023;14:933. https://doi.org/10.3390/genes14040933.
22. Zhu Y, Chen X, Lu Y, Xia L, Fan S, Huang Q, *et al.* Glutamine mitigates murine burn sepsis by supporting macrophage M2 polarization through repressing the SIRT5-mediated desuccinylation of pyruvate dehydrogenase. *Burns Trauma* 2022;10:tkac041. https://doi.org/10.1093/burnst/tkac041.
23. Wu H, Chen QY, Wang WZ, Chu S, Liu XX, Liu YJ, *et al.* Compound sophorae decoction enhances intestinal barrier function of dextran sodium sulfate induced colitis via regulating notch signaling pathway in mice. *Biomed Pharmacother* 2021;133:110937. https://doi.org/10.1016/j.biopha.2020.110937.
24. Casanova-Maldonado I, Arancibia D, Lois P, Peña-Villalobos I, Palma V. Hyperbaric oxygen treatment increases intestinal stem cell proliferation through the mTORC1/S6K1 signaling pathway in Mus musculus. *Biol Res* 2023;56:41. https://doi.org/10.1186/s40659-023-00444-3.
25. Tang J, Chen L, Qin ZH, Sheng R. Structure, regulation, and biological functions of TIGAR and its role in diseases. *Acta Pharmacol Sin* 2021;42:1547–55. https://doi.org/10.1038/s41401-020-00588-y.
26. Chen X, Zhang P, Zhang Y, Fan S, Wei Y, Yang Z, *et al.* Potential effect of glutamine in the improvement of intestinal stem cell proliferation and the alleviation of burn-induced intestinal injury via activating YAP: a preliminary study. *Nutrients* 2023;15:1766. https://doi.org/10.3390/nu15071766.
27. Madan E, Gogna R, Kuppusamy P, Bhatt M, Pati U, Mahdi AA. TIGAR induces p53-mediated cell-cycle arrest by regulation of RB-E2F1 complex. *Br J Cancer* 2012;107:516–26. https://doi.org/10.1038/bjc.2012.260.
28. Ni W, Yao S, Zhou Y, Liu Y, Huang P, Zhou A, *et al.* Long noncoding RNA GAS5 inhibits progression of colorectal cancer by interacting with and triggering YAP phosphorylation and degradation and is negatively regulated by the m(6)a reader YTHDF3. *Mol Cancer* 2019;18:143. https://doi.org/10.1186/s12943-019-1079-y.
29. Han S, Lim JY, Cho K, Lee HW, Park JY, Ro SW, *et al.* Anticancer effects of YAP inhibitor (CA3) in combination with Sorafenib against hepatocellular carcinoma (HCC) in patient-derived multicellular tumor spheroid models (MCTS). *Cancers* 2022;14:2733. https://doi.org/10.3390/cancers14112733.
30. Li D, Wang Y, Dong C, Chen T, Dong A, Ren J, *et al.* CST1 inhibits ferroptosis and promotes gastric cancer metastasis by regulating GPX4 protein stability via OTUB1. *Oncogene* 2023;42:83–98. https://doi.org/10.1038/s41388-022-02537-x.
31. He BF, Wu YX, Hu WP, Hua JL, Han Y, Zhang J. ROS induced the Rab26 promoter hypermethylation to promote cigarette smoking-induced airway epithelial inflammation of COPD through activation of MAPK signaling. *Free Radic Biol Med* 2023;195:359–70. https://doi.org/10.1016/j.freeradbiomed.2023.01.001.
32. Takeshima H, Niwa T, Yamashita S, Takamura-Enya T, Iida N, Wakabayashi M, *et al.* TET repression and increased DNMT activity synergistically induce aberrant DNA methylation. *J Clin Invest* 2020;130:5370–9. https://doi.org/10.1172/JCI124070.
33. Rasmussen KD, Helin K. Role of TET enzymes in DNA methylation, development, and cancer. *Genes Dev* 2016;30:733–50. https://doi.org/10.1101/gad.276568.115.
34. Ke J, Bian X, Liu H, Li B, Huo R. Edaravone reduces oxidative stress and intestinal cell apoptosis after burn through up-regulating miR-320 expression. *Mol Med* 2019;25:54.
35. Jacob S, Herndon DN, Hawkins HK, Enkhbaatar P, Cox RA. Xanthine oxidase contributes to sustained airway epithelial oxidative stress after scald burn. *Int J Burns Trauma* 2017;7:98–106.
36. Parihar A, Parihar MS, Milner S, Bhat S. Oxidative stress and anti-oxidative mobilization in burn injury. *Burns J Int Soc Burn Inj* 2008;34:6–17. https://doi.org/10.1016/j.burns.2007.04.009.

37. Prabhakaran HS, Hu D, He W, Luo G, Liou YC. Mitochondrial dysfunction and mitophagy: crucial players in burn trauma and wound healing. *Burns Trauma* 2023;11:tkad029. https://doi.org/10.1093/burnst/tkad029.
38. Park E, Chung SW. ROS-mediated autophagy increases intracellular iron levels and ferroptosis by ferritin and transferrin receptor regulation. *Cell Death Dis* 2019;10:822. https://doi.org/10.1038/s41419-019-2064-5.
39. Chen L, Zhang Z, Hoshino A, Zheng HD, Morley M, Arany Z, *et al*. NADPH production by the oxidative pentose-phosphate pathway supports folate metabolism. *Nat Metab* 2019;1:404–15. https://doi.org/10.1038/s42255-019-0043-x.
40. Jiang LB, Cao L, Ma YQ, Chen Q, Liang Y, Yuan FL, *et al*. TIGAR mediates the inhibitory role of hypoxia on ROS production and apoptosis in rat nucleus pulposus cells. *Osteoarthr Cartil* 2018;26:138–48. https://doi.org/10.1016/j.joca.2017.10.007.
41. Xiao Z, Deng S, Liu H, Wang R, Liu Y, Dai Z, *et al*. Glutamine deprivation induces ferroptosis in pancreatic cancer cells. *Acta Biochim Biophys Sin* 2023;55:1288–300. https://doi.org/10.3724/abbs.2023029.
42. Liu MY, Li HM, Wang XY, Xia R, Li X, Ma YJ, *et al*. TIGAR drives colorectal cancer ferroptosis resistance through ROS/AMPK/SCD1 pathway. *Free Radic Biol Med* 2022;182:219–31. https://doi.org/10.1016/j.freeradbiomed.2022.03.002.
43. Seo Y, Park SY, Kim HS, Nam JS. The hippo-YAP signaling as guardian in the pool of intestinal stem cells. *Biomedicine* 2020;8:560. https://doi.org/10.3390/biomedicines8120560.
44. Moya IM, Halder G. Hippo-YAP/TAZ signalling in organ regeneration and regenerative medicine. *Nat Rev Mol Cell Biol* 2019;20:211–26. https://doi.org/10.1038/s41580-018-0086-y.
45. Pobbati AV, Hong W. A combat with the YAP/TAZ-TEAD oncoproteins for cancer therapy. *Theranostics* 2020;10:3622–35. https://doi.org/10.7150/thno.40889.
46. Cunningham R, Hansen CG. The hippo pathway in cancer: YAP/TAZ and TEAD as therapeutic targets in cancer. *Clin Sci (Lond)* 2022;136:197–222. https://doi.org/10.1042/CS20201474.
47. Tang Y, Kwon H, Neel BA, Kasher-Meron M, Pessin JB, Yamada E, *et al*. The fructose-2,6-bisphosphatase TIGAR suppresses NF-$\kappa$B signaling by directly inhibiting the linear ubiquitin assembly complex LUBAC. *J Biol Chem* 2018;293:7578–91. https://doi.org/10.1074/jbc.RA118.002727.
48. Ganapathy-Kanniappan S, Geschwind JF. Tumor glycolysis as a target for cancer therapy: progress and prospects. *Mol Cancer* 2013;12:152. https://doi.org/10.1186/1476-4598-12-152.
49. Li X, Yang Y, Zhang B, Lin X, Fu X, An Y, *et al*. Lactate metabolism in human health and disease. *Signal Transduct Target Ther* 2022;7:305. https://doi.org/10.1038/s41392-022-01151-3.
50. Jafri F, Seong G, Jang T, Cimpeanu E, Poplawska M, Dutta D, *et al*. L-glutamine for sickle cell disease: more than reducing redox. *Ann Hematol* 2022;101:1645–54. https://doi.org/10.1007/s00277-022-04867-y.
51. Kim JS, Martin MJ. REDOX REDUX? Glutamine, catabolism, and the urea-to-creatinine ratio as a novel nutritional metric. *Crit Care Med* 2022;50:1156–9. https://doi.org/10.1097/CCM.0000000000005520.
52. Gong ZY, Yuan ZQ, Dong ZW, Peng YZ. Glutamine with probiotics attenuates intestinal inflammation and oxidative stress in a rat burn injury model through altered iNOS gene aberrant methylation. *Am J Transl Res* 2017;9:2535–47.
53. Wu Q, Ni X. ROS-mediated DNA methylation pattern alterations in carcinogenesis. *Curr Drug Targets* 2015;16:13–9. https://doi.org/10.2174/1389450116666150113121054.
54. Wang L, Mao B, Fan K, Sun R, Zhang J, Liang H, *et al*. ROS attenuates TET2-dependent ZO-1 epigenetic expression in cerebral vascular endothelial cells. *Fluids Barriers CNS* 2022;19:73. https://doi.org/10.1186/s12987-022-00370-8.